Flow (2026), **6** E5
doi:10.1017/flo.2026.10042

FLOW CAMBRIDGE UNIVERSITY PRESS

RESEARCH ARTICLE

Flow over a cylinder with a small triangular bump

Jack Elliott[1], Alex Nielson[2] and Barton L. Smith[2]

[1]Department of Integrated Engineering, Minnesota State University, Mankato, MN, USA
[2]Department of Mechanical and Aerospace Engineering, Utah State University, Logan, UT, USA
Corresponding author: Jack Elliott; Email: jack.elliott.2@mnsu.edu

Received: 4 August 2025; **Revised:** 23 December 2025; **Accepted:** 16 January 2026

Keywords: bluff body aerodynamics; boundary layer control; boundary layer separation

Abstract

The surface pressure distribution over a circular cylinder with a small, full-span, triangular bump is examined. The geometry of the bump is an isosceles triangle, the height of which is varied from 1.33 % to 5.33 % of the diameter of the cylinder and positioned between 60° and 120°. The Reynolds number ($Re = V_\infty D/\nu$, where V_∞ is the velocity of the freestream, D is the diameter of the cylinder and ν is the kinematic viscosity) is varied between 1.1×10^5 and 1.8×10^5. The lift and drag are estimated through the surface integral of pressure over the cylinder. The results show that the smallest bump acts as a trip for the lower Re and orientations before 70°, leading to a separation farther upstream than in the case of no bump. For larger bumps, Re and orientation angles, the bump acts as a spoiler and fully separates the boundary layer at the bump. In addition, the surface pressure upstream of the bump is strongly dependent on the bump position. The lift is highest for bump position less than 90° and decreases significantly with increasing bump location angle. The drag is less sensitive to the position of the bump. These findings have implications for predicting the forces on bluff bodies due to small asymmetric surface geometry features and extension to applications such as atmospheric flow over topography.

Impact Statement

Motivated by issues with existing baseball aerodynamics models, this experimental study investigated the influence of small asymmetric surface protrusions on cylinder aerodynamics near the critical Reynolds number. The researchers gathered wind tunnel measurements of the pressure over a circular cylinder with a small triangular bump, which demonstrate that the bump introduces a local favourable and then adverse pressure gradient. This reduces the near-wall momentum of the flow, and for small a bump close to the stagnation point, this develops the boundary layer. When a larger bump is farther from the stagnation point, the boundary layer fully separates from the surface. Across the full range of observations, the bump strongly influences the upstream pressure distribution but has less effect on the downstream pressure distribution. These findings provide a foundation for predicting the pressure distribution and resulting aerodynamic forces on baseballs and offer insights for similar bodies with small asymmetric surface geometries.

1. Introduction

Spoilers, also known as "lift dumpers," are flow-control surfaces that significantly alter the aerodynamic forces on an airfoil or similar shape by fully separating the attached boundary layer from the suction surface. These control devices are often seen on the upper surface of large aircraft wings, as shown in figure 1(*a*), and are used to reduce lift for descent or upon landing. A recent study on baseball aerodynamics (Smith *et al.*, 2024) showed that baseball seams act as spoilers when they lie near a plane through

© The Author(s), 2026. Published by Cambridge University Press. This is an Open Access article, distributed under the terms of the Creative Commons Attribution licence (https://creativecommons.org/licenses/by/4.0/), which permits unrestricted re-use, distribution and reproduction, provided the original article is properly cited.

https://doi.org/10.1017/flo.2026.10042 Published online by Cambridge University Press

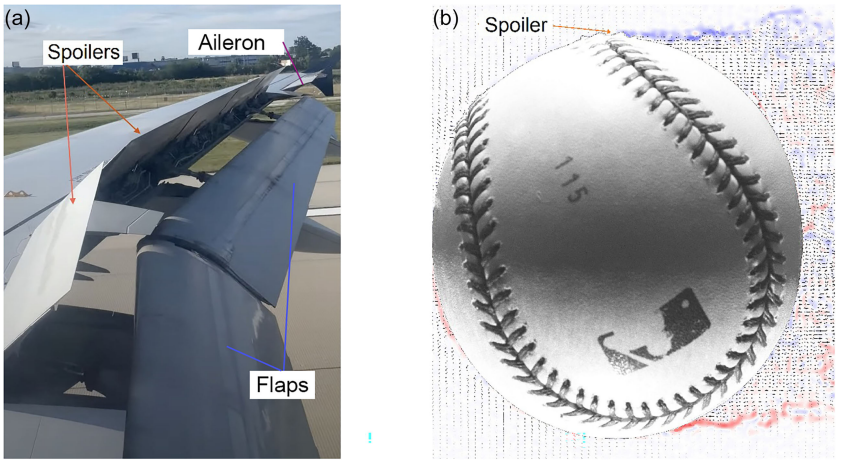


Figure 1. *(a) Commercial aircraft spoiler deployed at landing to eliminate lift and ensure that the aircraft remains on the ground. (b) A flow visualisation result with vorticity in colour demonstrating a baseball seam acting as a spoiler, indicated by boundary-layer separation and ensuing shear layer at the seam on top. Note that the boundary layer on the bottom side of the ball separates farther downstream.*

the centre of the ball and perpendicular to the direction of travel of the ball. At specific orientations, this can lead to a net force on a spinning baseball similar to, but in a different direction than, the Magnus effect (Briggs, 1959; Lyu *et al.*, 2022).

For the purpose of modelling the effect of baseball seams, it would be convenient to assume that the surface pressure behaves similarly to potential flow up to the separation point and then assumes the wake value. However, attempts to model forces on a baseball in this way, informed by experimentally determined separation points, have not been successful. The present study seeks to elucidate the pressure behaviour up and downstream of a small bump over a similar bluff body. To simplify the problem, a circular, non-spinning cylinder will be studied.

As a canonical flow, circular cylinders have been studied extensively. We will focus on the results for the Reynolds number range near the transition to turbulence. The first modern study on a circular cylinder in cross-flow is from Achenbach (1968). The surface pressure and shear stress of a smooth cylinder were measured in a range of Reynolds numbers similar to that of the present work. For $Re = V_\infty D/\nu = 10^5$, where V_∞ is the velocity of the free stream, D is the diameter of the cylinder and ν is the kinematic viscosity, they reported a laminar boundary-layer separation near $\theta = 78°$, where $\theta = 0$ is the stagnation point, as evidenced by the shear stress going to zero and the pressure assuming the base pressure value. For a larger Re of 2.6×10^5, the boundary layers remained laminar, but the separation point moved to $94°$. For $Re = 8.5 \times 10^5$, a laminar separation bubble formed behind the separation at $94°$ and reattachment. The final separation point was $147°$. For Reynolds numbers sufficiently large to cause turbulent boundary layers on the smooth cylinder ($Re = 3.6 \times 10^6$), the separation point was $115°$.

Three years later, Achenbach (1971) continued this work with measurements on uniformly roughened cylinders. A rough surface tends to move the "drag crisis," or the precipitous drop in drag owing to the transition to turbulence of the boundary layers and subsequent reduced wake, to lower values of Reynolds number. As the Reynolds number was increased further, drag was found to increase again to a value that became insensitive to Reynolds number. This final value was found to increase with surface roughness. The surface pressure on a rough cylinder was shown to be strong function of Reynolds number in the range $1 \times 10^5 < Re < 3 \times 10^6$. The present measurements are within this range.

Igarashi (1986) investigated the role of placing circular "tripping" wires on the surface of a circular cylinder in trans-critical cross-flow in a wind tunnel. These trips were placed symmetrically relative to the stagnation and the effects of relative roughness height and Re were measured through measurement of the Strouhal number, surface pressure distributions, smoke flow visualisation and oil film visualisation. These experiments demonstrated that the trips resulted in four "patterns" which are presented

https://doi.org/10.1017/flo.2026.10042 Published online by Cambridge University Press

in order of increasing *Re* for a given trip: (i) a laminar separation bubble, boundary-layer reattachment and laminar separation downstream of the reattachment; (ii) a laminar separation bubble, turbulent transition, turbulent boundary-layer reattachment and then turbulent separation; (iii) a laminar separation bubble, turbulent transition, turbulent boundary-layer reattachment and the turbulent separation point moves in the decreasing θ direction with increasing *Re*; and (iv) the turbulent boundary layer separates at the trip. These findings are similar to the findings of this study, but at a lower range of *Re* and with only symmetric "trips."

In Nebres & Batill (1993), a circular wire was added to the surface of a cylinder to examine the impact on the oscillation frequency of the wake. The surface pressure distribution that resulted from a wire 9 % of the diameter of the cylinder placed at various angles along the surface was also reported for $Re = 3 \times 10^4$. They found that when the wire was close to the stagnation point ($< 43°$), the wire caused separation and reattachment, leading to a final separation point far downstream than that of a smooth cylinder at this low Reynolds number. With the wire beyond this point, the wire caused boundary-layer separation, similar to the findings of this study.

The effect of roughness on the velocity profile of the boundary layer was reported by Güven *et al.* (1980). Generally, a smooth cylinder with a trip resulted in a more energetic boundary layer near the wall at the point of minimum pressure than the boundary layer on a cylinder with evenly distributed roughness. Similar results are observed for grooved surfaces (Seo *et al.*, 2013).

Nakamura & Tomonari (1982) investigated the difference between a "trip," as used in this study, and distributed roughness for flow over circular cylinders. Both of these changes to the cylinder move the drag crisis to lower values of *Re*. They concluded that a circular cylinder at Reynolds numbers as low as 3×10^5 can behave as trans-critical when a trip is employed around $50°$, but that distributed roughness results in a different behaviour. The findings of this study similarly show that the tripped pressure distribution is different from the pressure distribution for a uniformly roughened sphere at the same *Re*.

West & Apelt (1993) investigated pressure fluctuations on a smooth cylinder as a function of Reynolds number, turbulence level and blockage ratio. They found that the fluctuations were sensitive to Reynolds number and peaked near $Re = 8 \times 10^4$. In addition, these fluctuations reached their maximum near $\theta = 75°$.

Recent investigations into cylinders in cross-flow near the critical Reynolds number have included the work of Pasam *et al.* (2023), who considered the effect of relative roughness on cylinders with low blockage ratio to extend and improve on prior measurements of similar flows. Their results included a thorough set of data for this canonical flow to include mean and time-history pressures and forces, wake velocity distributions and momentum thicknesses. The data demonstrate a collapse of the base pressure, Strouhal number, Reynolds number, and wake angle with $Re_k = \rho V_\infty k/\mu$ for post-critical flows, where ρ represents the air density and k represents the roughness height. Similarly, Desai *et al.* (2020) combined surface pressure measurements and particle image velocimetry data from the wake to identify an antisymmetric and a symmetric mode in the cylinder wake. The antisymmetric mode, responsible for the von Kármán vortex shedding, decreased relative to the symmetric mode as the flow transitioned from trans-critical to critical.

Many flow features including transition of a cylinder in cross-flow may be controlled passively by modifying the cylinder surface. Choi *et al.* (2008) present a comprehensive review of passive control over bluff bodies, including circular cylinders. One relevant example discussed was a helical strake, or wire wrapped around a cylinder to prevent coherent vortex shedding from occurring over the full cylinder. Similar vortex shedding mitigation devices include spoiler plates, small plates normal to the surface distributed uniformly around the cylinder (Bianchi *et al.*, 2020).

Chopra and Mittal (2022) conducted a large eddy simulation of a cylinder with two trip heights (0.25 % and 1.0 % the cylinder diameter,) for *Re* from 2×10^3 to 5×10^5. These observations sought to better understand the "patterns" A, B/C and D in Igarashi (1986) and included a trip placed on a single side, with a smooth cylinder on the other. This selection was in part motivated by the relative lack of asymmetric trip locations in the prior literature which similarly motivates the present study. Results demonstrated that the boundary layer undergoes either natural transition through the formation of the

https://doi.org/10.1017/flo.2026.10042 Published online by Cambridge University Press

laminar separation bubble for the smallest trip, or direct transition for the largest trip. A two-stage drag crisis was observed, owing to the boundary-layer transition on the opposite sides occurring at different values of Re.

In Lin *et al.* (2025), a device described as a "spoiler" was used to passively control the flow around a rectangular cylinder. The spoilers were plates on the leading edge of the rectangular cylinder angled 45° with respect to the surface of the cylinder. The effect of the spoilers on lift and drag as well as the time evolution of the flow was investigated. A recent example of passive flow control on a cylinder can be found in Gong *et al.* (2024). They reported that cylinder drag can be reduced by placing a small rod parallel to and behind the cylinder. Other locations were also tested.

Small spoilers have also been considered as one of several alternatives to control flow separation in many aerodynamics applications. Small rectangular "mini spoilers" or "mini tabs" protruding controllable extents normal from a leading or trailing edge of an airfoil have recently been demonstrated as a means to control aerodynamic forces on a wing (Blaylock *et al.*, 2014; Heathcote *et al.*, 2020) without the elaborate design requirements and slow response time typical for larger spoilers (figure 1*a*). Similarly, spoilers and synthetic jets (Smith & Glezer, 1998) are flow-control methods to actively separate the boundary layer and reduce dynamic stall in gust and/or flapping conditions (Barnes, 2024; Qian *et al.*, 2023).

Spoilers have also emerged as a method for improving hydraulic turbine designs. Specifically, Bourgeois & Houde (2023) numerically investigated spoilers as a means to limit discharge for spin no-load turbines. This study identified that the spoilers were effective in increasing head loss at the turbine as desired.

Finally, devices also referred to as spoilers have been applied in piping systems with closed-branch T-junctions to reduce pulsations due to the resonating acoustic field with periodic vortex shedding at the junction(s) (Bruggeman *et al.*, 1989). In this context, Bruggeman *et al.* (1991) identified a pulse reduction of 30–40 dB by placing a spoiler upstream of a second T-junction in cases where pulsations depend more on the absorption of the shed vortex energy than shear-layer stabilisation. The spoilers did not reduce pulsations when placed upstream of the first junction, and are limited in other T-junction cases by the relative importance of shear-layer stability (Botros *et al.*, 2022).

However, these devices act to disrupt the boundary layer and do not necessarily fully separate the boundary layer from the surface. Due to this ambiguity, this manuscript will maintain the language of "bump" to describe the selected geometries extending from the cylinder surface. The term "spoiler" will be reserved for cases where the bump acts to fully separate the boundary layer. The term "trip" will be reserved for cases where the bump does not fully separate the boundary layer.

Overall, these studies demonstrate the dependence of the separation location on the small surface features and the potential for trips and spoilers as a flow-control method in a variety of applications. However, the literature regarding the influence of small, asymmetrically placed spanwise surface features on a circular cylinder is underdeveloped. Specifically, the influence of a small ($1\,\% \leq \delta \leq 5\,\%$,) triangular bump, placed on a single side of a circular cylinder, similar to the geometry of a baseball seam, has not been experimentally observed. Thus, the present study examines the effect of a small, triangular-shaped bump on the surface pressure due to flow over a cylinder. In what follows, we will first describe the experimental set-up. This will be followed by results, a discussion of the results and conclusions.

2. Experimental set-up

2.1. Test article

The test article was a 75-mm-diameter, smooth aluminium cylinder with a 5-mm slot milled in the longitudinal direction. This slot received one of the 3-D printed bumps as shown in figure 2. The bumps are isosceles triangle cross-sections, with 10-mm end-to-end width in the direction tangent to the cylinder surface, and protrusion(s) 1-, 2- and 4-mm in the direction normal to the cylinder surface, beginning at the cylinder surface. The surface pressure distribution was measured as a function of Reynolds number, bump size and bump position.

https://doi.org/10.1017/flo.2026.10042 Published online by Cambridge University Press

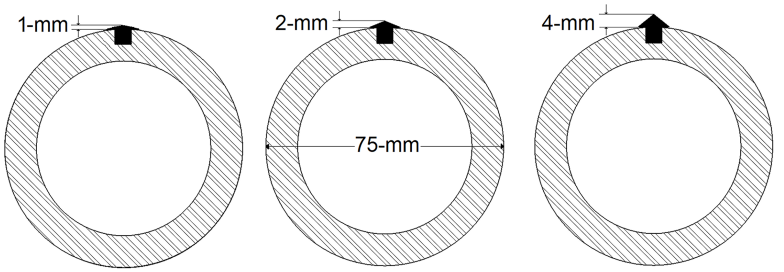


Figure 2. *Schematics of the three bump geometries used in this study. The bumps were isosceles-triangle-shaped with 10-mm width and protruded from the 75-mm diameter cylinder 1-, 2- and 4-mm.*

The relative bump sizes δ are 1.33 %, 2.66 % and 5.33 % of the cylinder diameter. We note that baseball seams, which motivate this study, are approximately 1 % of the diameter of a baseball. The most similar study the authors identified of a bump on the surface of a cylinder included circular cross-section bumps that were much larger: $\delta \geq 9\,\%$ (Nebres & Batill, 1993).

2.2. Free-stream flow field

The cylinder was mounted in an Engineering Lab Designs 407A recirculating wind tunnel with a 0.6×0.6-m test section. The manufacturer's specification for streamwise turbulence intensity level is ≤ 0.25 % of the mean tunnel velocity V_∞.

The Reynolds number range investigated in this study is less than a factor of two. However, we note that the flow is quite sensitive to the Reynolds number in this range. The maximum value was chosen to match the baseline case of the baseball study by Smith *et al.* (2024). The minimum value was selected to represent the lower limit of baseballs pitched in competitive sports (i.e., secondary school-age pitchers). For each test, the tunnel was started for 30 s before data collection to ensure that the free-stream velocity was in steady state for the target value of Reynolds number.

Barometric pressure and ambient temperature were measured daily to find the air density and viscosity. Due to the large number of samples for the time-averaged method of setting Reynolds number, the random uncertainty of the mean is insignificant.

We note that the tunnel temperature increased with time ($\Delta T < 5\,^\circ$C per test). As this affects the viscosity and density used in the *Re* calculation, we continuously compensated for changes in tunnel temperature with changes in tunnel velocity to maintain a fixed *Re* value. The tunnel was also allowed to cool between each test.

Acrylic discs of 150-mm diameter were mounted above and below the measurement section to suppress spanwise flow. Zig-zag turbulent trips at 45° from the stagnation point ensure that the boundary layer is turbulent at separation. The trips spanned the measurement section and were 0.25-mm tall, 6-mm peak-to-peak and 9-mm in the lateral direction. The cylinder spanned the height of the test section, resulting in a blockage ratio of 12 %. Figure 3(*a*) shows the cylinder mounted in the test section.

2.2.1. Free-stream flow field uncertainty

Temperature variations are sources of systematic error; the density may vary by 1.67×10^{-2} kg m^{-3} and the viscosity by 2.37×10^{-7} kg m^{-1} s^{-1}. In addition, the wind tunnel velocity was calculated using a Pitot probe in the entrance to the test section connected to differential pressure transducers: $V = \sqrt{2\Delta P/\rho}$. One transducer was used for pressure differences up to 750 Pa and a second transducer for pressure differences up to 3.7 kPa. The calibration certificate uncertainties for these transducers are 0.5 % of full scale.

https://doi.org/10.1017/flo.2026.10042 Published online by Cambridge University Press

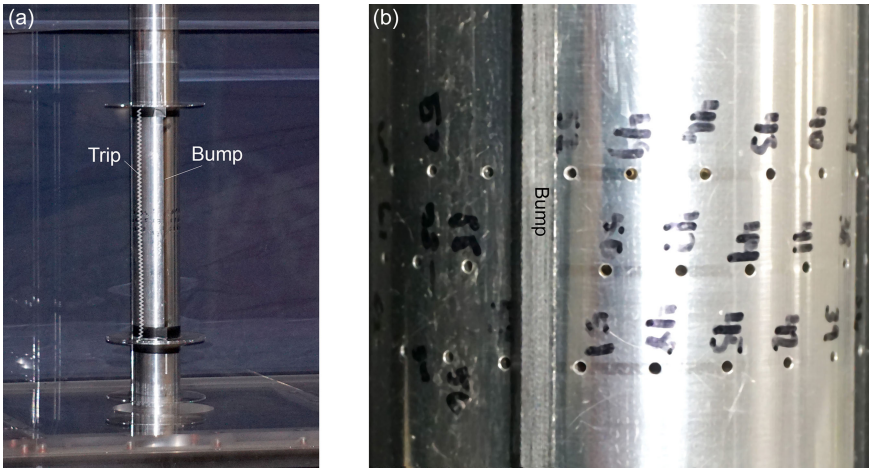


Figure 3. *(a) Cylinder mounted in the wind tunnel test section showing the acrylic disks, the trip and the three rows of pressure ports. (b) Close up of the cylinder on the bench showing the three rows of pressure ports and the largest bump. Note that the trip is not applied in this image.*

To estimate the total uncertainty in the Reynolds numbers, we propagated these individual uncertainties using the Taylor series method (Coleman & Steele, 2009; Smith & Neal, 2025) for the data reduction equation: $Re = D\sqrt{2\rho\Delta P}/\mu$

$$u_{Re} = \sqrt{\left(\frac{D\sqrt{\Delta P}}{\mu\sqrt{2\rho}}u_\rho\right)^2 + \left(\frac{D\sqrt{\rho}}{\mu\sqrt{2\Delta P}}u_{\Delta P}\right)^2 + \left(\frac{\sqrt{2\rho\Delta P}}{\mu}u_D\right)^2 + \left(\frac{D\sqrt{2\rho\Delta P}}{\mu^2}u_\mu\right)^2 + 2\left(\frac{D^2\Delta P}{\mu^3}u_\rho u_\mu\right)}. \quad (1)$$

Temperature measurements were made using the same instrument, and we treat their errors as perfectly correlated $u_{\rho\mu} = u_\rho u_\mu$ according to the recommendation of Coleman & Steele (2009). This method provides the total uncertainty as 1.2×10^4, 2.5×10^4 and 2.6×10^4 for the Reynolds numbers 1.1×10^5, 1.3×10^5 and 1.8×10^5, respectively. We note that the contribution of the uncertainty from the pressure transducers is an order of magnitude larger than the combined contributions of the uncertainties of all other terms (D, ρ and μ).

2.2.2. Test article orientation uncertainty

We varied the bump position by rotating the cylinder on a lathe chuck which held the cylinder from below. The bump orientation measurements were based on aligning the longitudinal slot location with a protractor, which was fixed to the access port of the test section used to mount the cylinder. The protractor was aligned with the free stream through parallel lines to the test section walls and verified by rotating the cylinder to identify maximum (stagnation) pressure at the expected angle. Thus, we estimate the upper limit for the uncertainty of the angular location (θ) as half the resolution of the pressure ports placed every $5°$: $u_\theta = 2.5°$. This mounting method also pressed the top of the cylinder against the top of the wind tunnel test section to eliminate vibration.

The range of bump locations for this study were limited by the presence of turbulent trips (that is, $\theta_b = 60°$) to the last value before the fully separated region (that is, $\theta_b = 120°$) and varied in increments of $10°$.

2.3. Pressure measurements

The pressure ports were 0.79-mm diameter holes drilled every $5°$ around the circumference of the cylinder (figure 3*b*). Brass tubes connected a plastic hose to each internal hole in the cylinder, and these hoses

https://doi.org/10.1017/flo.2026.10042 Published online by Cambridge University Press

extended through the cylinder to a slot in the top of the wind tunnel test section. The hoses were then connected to the pressure sensor. The static port on the Pitot-static probe mounted at the entrance of the test section provided the static pressure p_∞. Tunnel velocity was measured using the same Pitot-static probe and a separate differential pressure sensor.

The pressure difference for each port was measured by sampling the output voltage of a 100 Torr capacitance manometer connected to the desired port on the cylinder surface and the static port for 30 s at 100 Hz. From these data, the pressure coefficient $C_p = 2(p - p_\infty)/\rho V_\infty^2$ was determined. We assume that the values for computing C_p from the pressure difference measurement are fixed at a given value of *Re*. Thus, to convert pressure difference measurements to C_p, we identified the constant required at each observed *Re* for the pressure coefficient to provide $C_p = 1$ at $\theta = 0°$. These observations were made with the bump positioned in the wake ($\theta_b = 180°$) to eliminate the potential influence of the bump. Through this method, we did not include ρ or V_∞ directly to compute C_p.

To correct these measurements in confined flow according to the moderate blockage (the blockage ratio $B = 12\%$) for the cylinder in the trans-critical regime (i.e., $1.1 \times 10^5 \leq Re\ 1.8 \times 10^5$), we applied the momentum correction method developed by Maskell (1963) and validated by Farell *et al.* (1977). Specifically, we used each measured C_{pm} to find the unconfined *corrected* surface pressure coefficient C_p by first defining the base pressure parameter k, which is related to the base pressure coefficient C_{pb} through $k^2 = 1 - C_{pb}$. This parameter relates the measured (indicated by subscript m) base pressure parameter $k_m^2 = 1 - C_{pbm}$ to the corrected base pressure parameter $k_c^2 = 1 - C_{pbc}$ where the corrected value k_c is identified for iteration n using

$$(k_c^2)_n = \frac{k_m^2}{1 + \frac{BC_{D1}}{(k_c^2)_{n-1} - 1}}. \tag{2}$$

We neglected the skin friction drag, which is relatively small for cylinders in the trans-critical regime, and numerically integrated the surface pressure to identify C_D. This method was iterated until the parameter converged at $(k_c^2)_n - (k_c^2)_{n-1} < 1 \times 10^{-6}$. Then, we applied the ratio of measured to corrected dynamic pressures to identify the corrected base pressure, the corrected dynamic pressure, and the corrected surface pressure(s)

$$\frac{q_c}{q_m} = 1 + \frac{B}{(C_{pb})_c} = \frac{C_{pc}}{C_p}. \tag{3}$$

In this study, the momentum-method-corrected values for the surface pressure, the resulting lift and the resulting drag coefficients are reported. The uncorrected values are omitted to maintain consistency.

2.3.1. Surface pressure measurement uncertainty

The capacitance manometer resolution is 10^{-6} of full scale (100 Torr). The lowest *Re* at the mean measured density of 1.006 kg m^{-3} and velocity of 26.55 ms^{-1} provides the minimum dynamic pressure of 2.66 Torr, which is 2.66 % of the full range. Converting to C_p yields a resolution in pressure coefficient of 3.76×10^{-5} and a 68 % confidence random uncertainty due to resolution limits of half the resolution: 1.88×10^{-5}. Time averaging the 3,000 samples per measurement is sufficient to render the random uncertainty of the mean ($u_{r,C_p} = 1 \times 10^{-3}$) insignificant.

Given the excellent pressure instrument, we claim that the main source of uncertainty in this measurement is the error in the stagnation pressure value due to the misalignment of the measurement port with $\theta = 0°$. Assuming that the pressure near stagnation follows the potential flow solution, we estimate that the maximum error due to misalignment of the port at $\theta = 0°$ is $\pm\ 1 - C_p(2.5°) = 0.01$. To evaluate repeatability, the baseline case of the bump oriented at 180° and $Re = 1.8 \times 10^5$ was measured on two separate days. The mean surface pressure measurement differences across days were less than the pressure measurement uncertainty due to port misalignment. Thus $u_{C_p} = 0.01$ at a 68 % confidence random uncertainty.

https://doi.org/10.1017/flo.2026.10042 Published online by Cambridge University Press

Table 1. *Experimental parameters*

Parameter	Values
Re ($\times 10^5$)	1.1, 1.3, 1.8
Bump orientation θ_b (°)	60– 120 in increments of 10
Bump relative size δ (%)	1.33, 2.66, 5.33

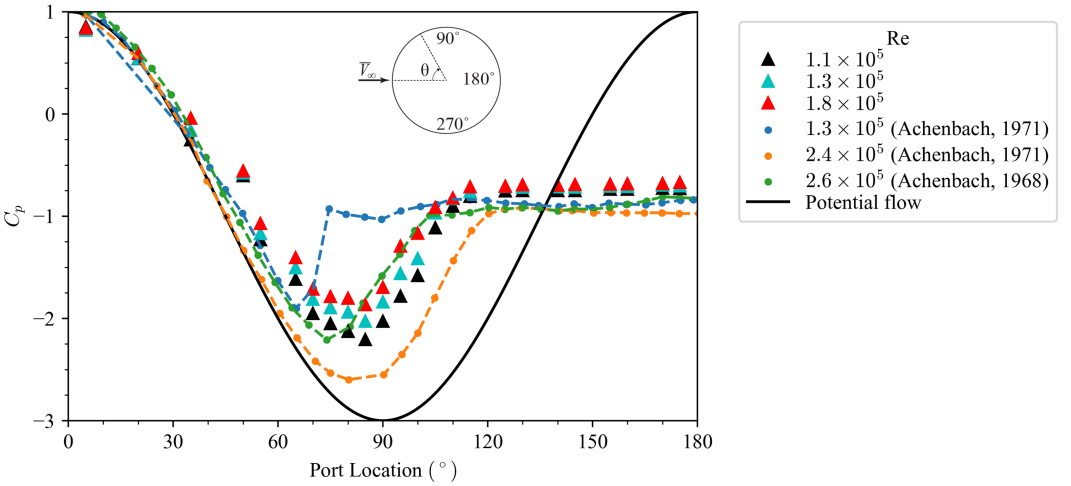


Figure 4. *Surface pressure coefficient as a function of angle with the bump at* 180° *for three values of Re. The black curve is the potential flow solution. Also included are results from a smooth cylinder study (Achenbach, 1968) and a uniformly roughened cylinder (Achenbach, 1971). Uncertainty bands are omitted to maintain readability.*

The full parameter space for this study is shown in table 1.

3. Results and discussion

3.1. Baseline pressure results

We begin by examining a case where the bump is at 180°, in the wake, and has no observable effect on the flow. This forms the baseline case. The surface pressure distributions for the three values of Reynolds number are shown in figure 4. Only one side of the cylinder is plotted since the surface pressure distribution is symmetric when the bump is located at 180°. The potential flow pressure distribution is included for reference. Examining the present results compared with the studies of Achenbach (1968, 1971), it is clear that the pressure distribution resulting from a tripped boundary layer on a smooth cylinder is not the same as that of a smooth or uniformly rough cylinder, as reported by Nakamura & Tomonari (1982).

For each *Re* value, stagnation pressure ($C_p = 1$) is experienced at $\theta = 0°$. Increasing *Re* results in more dissipation in the boundary layer. Compared with potential flow, the negative pressure gradient $-\mathrm{d}C_p/\mathrm{d}\theta$ is lower, and more so for larger Reynolds numbers, especially downstream of trips near 45°. Despite the increasing dissipation in the boundary layer with *Re*, the separation point does not change appreciably with *Re* and is near 110°. The base pressure (downstream of the separation point) is similar for each case with a value near $C_p = -0.75$.

3.2. The upstream effects of bump position and size

We now present the pressure data for the side of the cylinder with the bump. The range of bump locations is from 60°, which is as far upstream as possible to avoid interaction with the trip, to 120°, where the

https://doi.org/10.1017/flo.2026.10042 Published online by Cambridge University Press

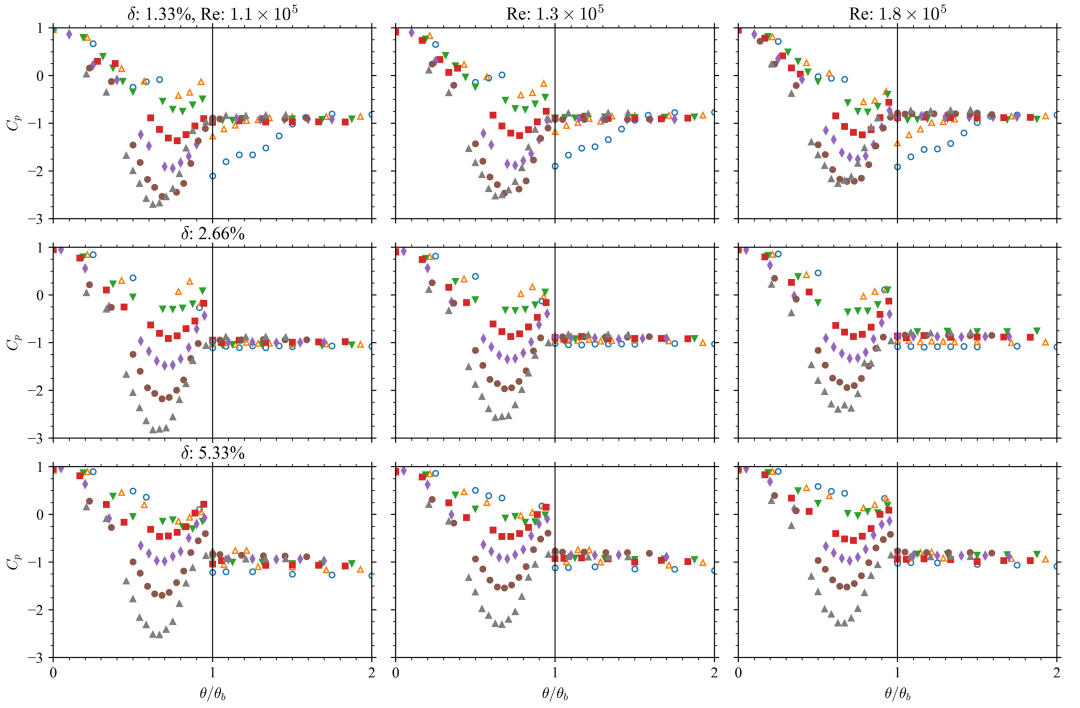


Figure 5. *Surface pressure coefficient as a function of the bump position divided by the bump position angle with the bump angles ranging from* 60° *to* 120° *for the three sizes and three values of Re. The bump positions are* 60° (○), 70° (△), 80° (▼), 90° (■), 100° (◆), 110° (●) *and* 120° (▲). *The solid lines at* $\theta/\theta_b = 1$ *indicate the bump location. Uncertainty bands are omitted to maintain readability.*

bump is at the edge of the wake and the spoiler does not influence the flow when positioned at greater angles. The pressure was not measured within 5° of the turbulent trip tape ($40° \leq \theta \leq 50°$) to avoid spurious values due to blockage and/or local pressure gradients. To visualise these observations more carefully, we transform the x-axis into the ratio of the pressure port angle to the bump angle: θ/θ_b (figure 5). Note that the non-transformed pressure data for all cases with a bump are presented in the Appendix.

Across all observations, the pressure distributions appear similar in the range $0 \leq \theta/\theta_b \leq 1$, and the pressure upstream of the bump is higher than the potential flow solution. This increase depends on the location of the bump. Generally, the pressure increases with a decrease in bump position angle (θ_b) and an increase in bump size. Similarly, the pressure upstream of the bump generally increases with an increase in the size of the bump.

Based on the results of the surface pressure distribution in figure 5, the bump can have one of two effects after the bump: $\theta/\theta_b > 1$, each likely due to the local favourable and then adverse pressure gradient generated by the bump geometry.

(i) Causing complete separation of the boundary layer, indicated by the constant surface pressure after the bump. This is referred to as the bump acting as a spoiler.

(ii) Causing thickening of the attached boundary layer or separation with reattachment. In these cases, the surface pressure decreases then increases after the bump until a final separation point farther upstream than in the baseline case. This is referred to as the bump acting as a trip.

These effects (i) and (ii) are respectively aligned with the "patterns" C and D presented in the smaller circular trip wire observations by Igarashi (1986). The mechanisms are further elaborated through the large eddy simulation study results by Chopra and Mittal (2022).

https://doi.org/10.1017/flo.2026.10042 Published online by Cambridge University Press

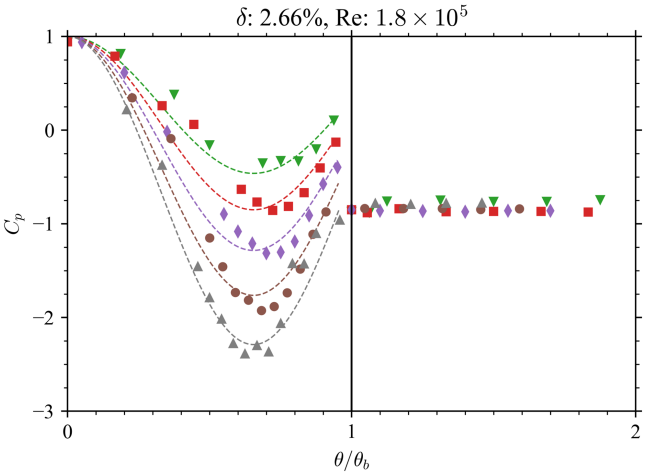


Figure 6. *Fitted model curves of surface pressure coefficient as a function of the bump position divided by the bump position angle with the bump angles ranging from* $80°$ *to* $120°$ *for* $Re = 1.8 \times 10^5$, $\delta = 2.66\,\%$. *The bump positions are* $80°$ *(▼),* $90°$ *(■),* $100°$ *(▼),* $110°$ *(●) and* $120°$ *(▲). The solid line at* $\theta/\theta_b = 1$ *indicates the bump location.*

3.3. Spoiler behaviour

We begin by discussing the range of bump locations that result in effect (i): the bump fully separates the boundary layer. For all *Re* values and all three sizes, the bump significantly increases the surface pressure upstream of the bump. This makes the pressure gradient more adverse than for the case of no bump at the same location. The pressure also increases upstream of the bump with an increase in bump size. Thus, we observe that a sufficiently large bump, positioned at a location where the bump creates an adverse pressure gradient, will act as a spoiler. We propose that this effect is due to a bump reducing the near-wall momentum to zero, fully separating the boundary layer. In this case, the pressure immediately increases to the base value after the bump. Figure 5 indicates that the bump acts as a spoiler for all observations except for the smallest bump ($\delta = 1.33\,\%$) placed at $\theta_b = 60°$ and $\theta_b = 70°$.

This is the effect observed in Smith *et al.* (2024), where a baseball seam was found to act like a spoiler. The range of angles where seams were found to have this effect was roughly the same as the present results. A simple model fits the pressure distribution upstream of the spoilers. We fitted a modified version of the inviscid potential flow solution for a circular cylinder: $C_p(\theta) = 1 - C_1\theta_b^2 sin^2(C_2\theta/\theta_b)$ to the data for $Re = 1.8 \times 10^5$, $\delta = 2.66\,\%$. Figure 6 presents the resulting pressure distributions according to the least-squares best-fit result: $C_p(\theta) = 1 - 0.75\theta_b^2 sin^2(2.4\theta/\theta_b)$.

We expect the fitted curve presented here to provide a next step in predicting the surface pressure over a baseball according to a known orientation, given the model is appropriately adjusted for differences in cylinders and spheres (Yeung, 2009).

3.4. Trip behaviour

We now consider the bump positions and sizes that result in effect (ii): the bump acts as a trip and does not fully separate the boundary layer. Rather, we expect that the bump acts similarly to an isolated roughness element by further developing the already turbulent boundary layer. Specifically, that the local favourable then adverse pressure gradient introduced by the bump decreases, but does not reduce to zero, the near-wall momentum of the boundary layer. This development is evidenced by complete separation at a lower value of θ than for the cylinder without the bump.

For the surface pressures observed at all values of *Re* in figure 5, the bump acts as a trip for the bump $\delta = 1.33\,\%$ placed at $\theta_b = 60°$ and for the bump $\delta = 1.33\,\%$ placed at $\theta_b = 70°$. To assist the discussion

https://doi.org/10.1017/flo.2026.10042 Published online by Cambridge University Press

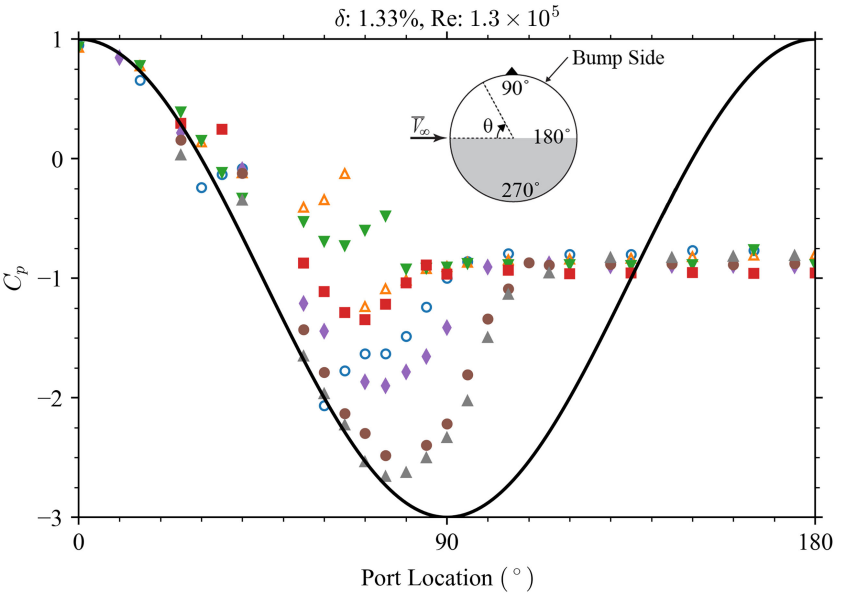


Figure 7. *Surface pressure coefficient as a function of the bump position ranging from* 60° *to* 120° *for* $\delta = 1.33\,\%$, *Re*= 1.1×10^5. *The bump positions are* 60° (○), 70° (△), 80° (▼), 90° (■), 100° (◆), 110° (●) *and* 120° (▲). *The black line is the potential flow solution.*

of the trip behaviour, figure 7 shows the non-transformed surface pressure data for the bump side of the cylinder for $\delta = 1.33\,\%$, $Re = 1.1 \times 10^5$.

As shown in figure 7, the flow reattaches downstream of the bump, evidenced by the large decrease in pressure after the bump location. For the case of the bump located at 60°, the pressure also coincides with the potential flow solution at the bump and increases with increasing θ until separation (indicated by constant surface pressure) near 90°. For the case of the bump located at 70° and size 1.33 %, the dissipation is higher than for the 60° case, but the final separation also occurs at 90° and the base pressure is the same for both positions.

These observations match the effect of roughness over supercritical spheres (Achenbach, 1972; Elliott *et al.*, 2024; Norman & McKeon, 2011). Further, this result is opposite to that observed for subcritical cylinders (Nebres & Batill, 1993), where a cylindrical "spoiler" delayed boundary-layer separation compared with the case of no spoiler by transitioning the boundary layer to turbulent. This difference is owed to the boundary layer in this study being tripped to turbulent by both the trip tape at 45° and the larger *Re* value. For the larger bumps at these positions $\theta_b \geq 60°$ ($\delta = 2.66\,\%$ and $5.33\,\%$), the bump acts as a spoiler as the boundary layer separates and remains detached downstream of the bump.

3.5. Non-bump side pressures

The surface pressure distribution on the side opposite the bump is insensitive to the bump position, with some notable exceptions. The first of these exceptions is observed in the case of the intermediate bump size ($\delta = 2.66\,\%$) at all values of Re, shown in figure 8. Here, the pressure on the non-bump side of the cylinder is increased in the region $240° \leq \theta \leq 270°$ compared with the other cases.

The opposite is seen for the largest bump $\delta = 5.33\,\%$ at the intermediate and highest Re: 1.3×10^5 and 1.8×10^5. Figure 9 shows the result for $Re = 1.3 \times 10^5$. Specifically, the boundary layer remains attached much farther in the streamwise direction than the other non-bump side cases for $\theta_b = 90°$. Further, the pressure in this region ($220° \leq \theta \leq 260°$) is lower than for the other cases which separate near the baseline separation point: $\theta = 240°$.

https://doi.org/10.1017/flo.2026.10042 Published online by Cambridge University Press

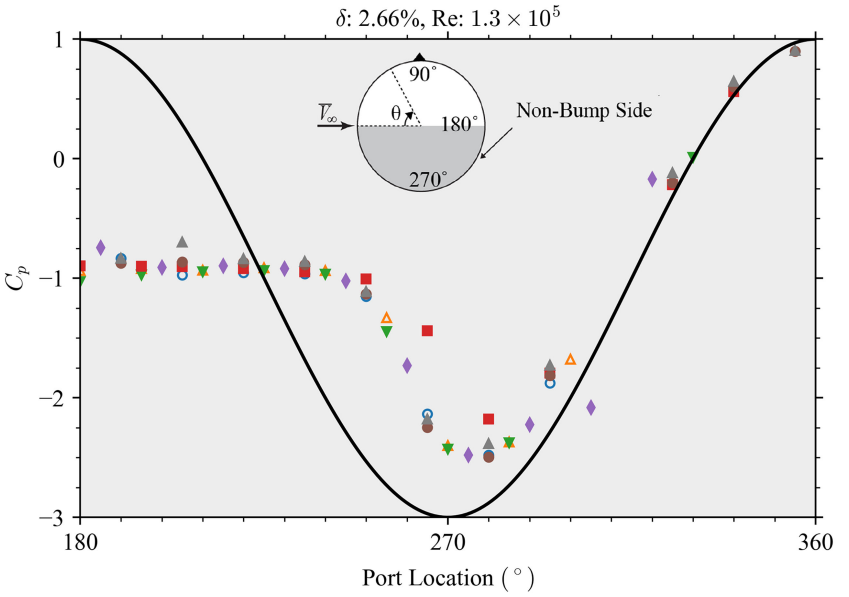


Figure 8. *Surface pressure coefficient on the side of the cylinder without the bump as a function of the bump position ranging from* 60° *to* 120° *for* $\delta = 2.66\,\%$, *Re*= 1.3×10^5. *The bump positions are* 60° (○), 70° (△), 80° (▼), 90° (■), 100° (◆), 110° (●) *and* 120° (▲). *The black line is the potential flow solution.*

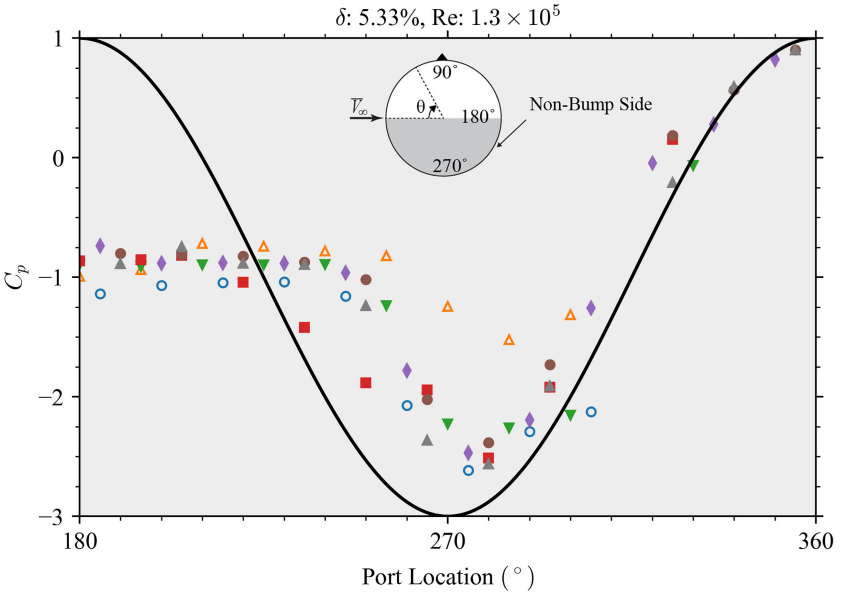


Figure 9. *Surface pressure coefficient on the side of the cylinder without the bump as a function of the bump position ranging from* 60° *to* 120° *for* $\delta = 5.33\,\%$, *Re* = 1.3×10^5. *The bump positions are* 60° (○), 70° (△), 80° (▼), 90° (■), 100° (◆), 110° (●) *and* 120° (▲). *The black line is the potential flow solution.*

In Smith *et al.* (2024), it was reported that when a baseball at *Re* = 1.8×10^5 has a seam near 90° and no seam on the opposite side of the sphere, the separation point moves toward a lower θ on the non-seam side. Specifically, the separation from a baseball is normally about 115° (245° in figure 8), but moves

https://doi.org/10.1017/flo.2026.10042 Published online by Cambridge University Press

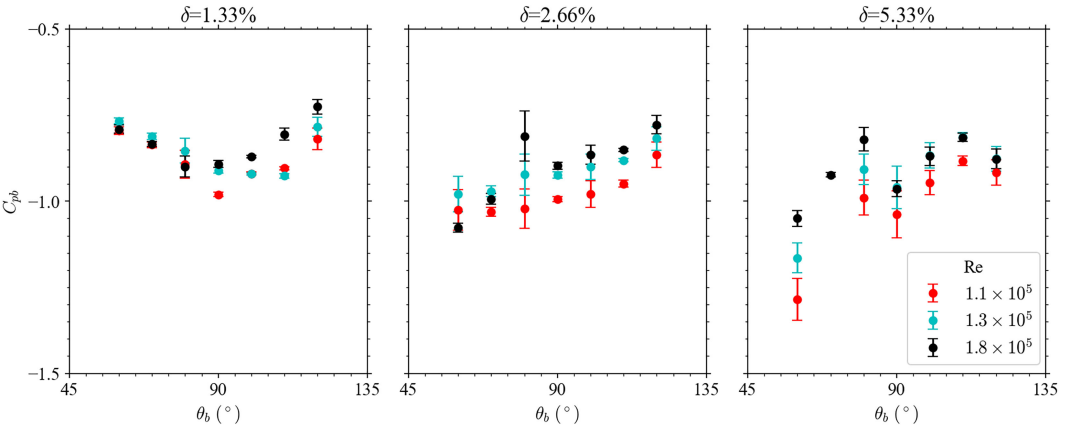


Figure 10. *Mean base pressure coefficient as a function of the bump position ranging from* 60° *to* 120° *for all three values of bump size and Re. The error bars represent the 95 % confidence random uncertainty of the mean.*

closer to 90° (270° in figure 8) when the seam is at 90°. In this study, there is evidence that the same is true for a cylinder for the 2-mm (2.66 %) bump. As shown in figure 8, the separation point moves back to the common value near 240° for any bump location other than $\theta_b = 90°$, similar to the baseball result.

3.6. Base pressure

To supplement the discussion of base pressure, we present the typical base pressure measured through the mean surface pressure coefficient in the range $120 \leq \theta \leq 240$. Figure 10 shows the base pressure data, organised by bump size and Re.

As shown in figure 10, the base pressure generally increases with an increase in bump angle for the larger bumps: $\delta = 2.66\,\%$ and $\delta = 5.33\,\%$. For the smallest bump, the base pressure decreases with an increase in θ_b to a local minimum at $\theta_b = 90°$. The base pressure increases with an increase in θ_b through the range of remaining observed bump angles. Interestingly, the lowest values for the base pressure are observed for the largest bump when the bump is oriented the furthest upstream, $\theta_b = 60°$. Finally, the base pressure generally increases with an increase in Re, which aligns with expectations for circular cylinders.

3.7. Aerodynamic force results

The impact of the bump on the lift and drag, which is a function of the pressure around the cylinder, is shown in figure 11. We note that the fluid forces integrated to form these coefficients are only pressure forces, but the contribution of skin friction is negligible in all directions. Achenbach (1971) notes that skin friction amounts to less than 2 % of the total drag for a rough cylinder.

Generally, a bump on one side of a cylinder leads to lift toward the opposite side. The only exception is the bump of 2.66 % at 120°, which can cause a force in the opposite direction. For the two smallest bump sizes, the highest lift value is for a bump on the front of the cylinder ($\theta_b < 90°$), while the pressure drag is not sensitive to the location of the bump.

The drag is less sensitive to the bump position. The largest changes in drag occur across the observed values of *Re* for the smallest bump at $\theta = 60°$ and $\theta = 70°$. The boundary layer is not fully separated at the bump. Rather, the boundary layer reattaches, corresponding to a significantly lower pressure value than the baseline and higher observations of θ_b. In the case of $\theta_b = 60°$, this leads to the lowest drag observed.

https://doi.org/10.1017/flo.2026.10042 Published online by Cambridge University Press

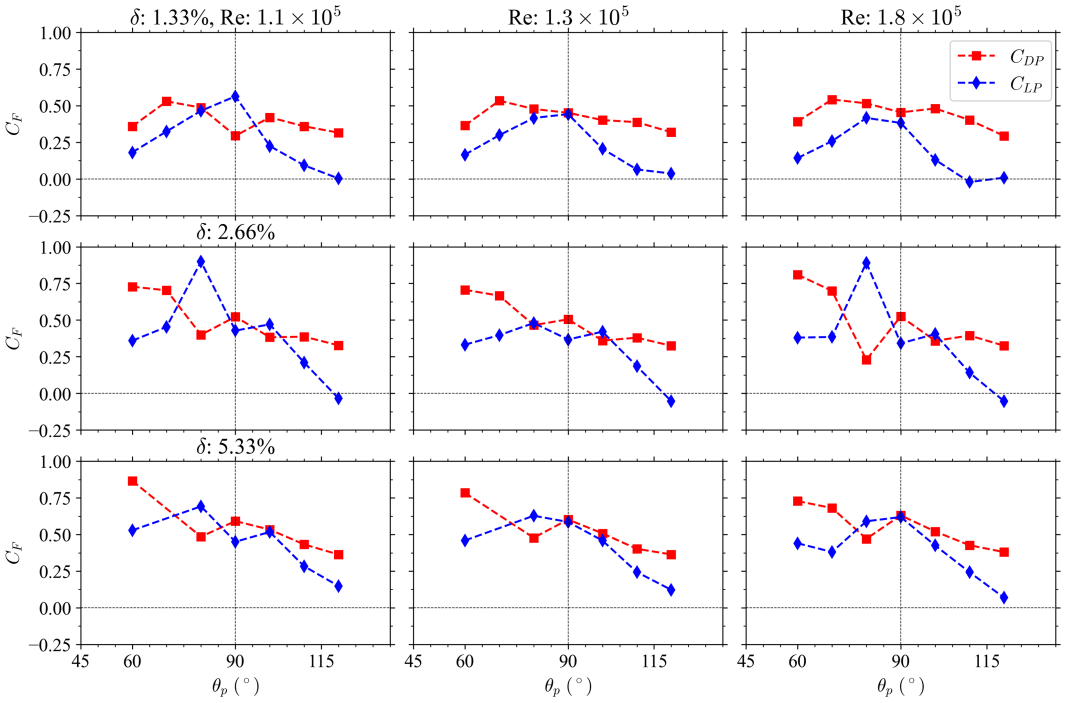


Figure 11. *Pressure integrated lift and drag coefficients as a function of bump position, size and Reynolds number. The force coefficients are integrated from the pressure coefficients, and thus have the same uncertainty* $u_{C_F} = 0.01$ *while the location uncertainty is* $u_{\theta_b} = 2.5°$.

The delayed separation for the largest bump at 90° does not result in increased lift and also comes with a large drag penalty. The drag can be seen to depend only weakly on the bump position. However, it is also clear that drag increases with bump size, and that the drag is lowest for the smallest bump positioned farthest upstream.

4. Conclusions and recommendations

An experimental study of a smooth, tripped cylinder equipped with a spanwise bump on one side is reported. The Reynolds number range ($1.1 \times 10^5 \leq Re \leq 1.8 \times 10^5$) is chosen to lie near the drag crisis. The main result reported here is surface pressure and the forces it generates.

The baseline flow (with the bump in the wake, where it has no influence) resembles previously reported results for smooth, tripped cylinders. Viscous dissipation in the boundary layer was shown to increase with Reynolds number, while the separation point is near 110° and the base pressure remains constant with Re.

The smallest bump tested was only 1.33 % of the cylinder diameter. Even so, the pressure upstream of the bump is strongly dependent on the bump position for all observations. Overall, the pressure upstream of the bump increases with an increase in bump size. The pressure upstream of the bump also increases the farther the bump is positioned upstream. The pressure distributions upstream of the bump appear similar when the cylinder location variable θ is transformed by the ratio to the bump position θ/θ_b. All three bumps removed the boundary layer from the surface when placed anywhere from 80° to 120°. As a result, the pressure distribution, and therefore the lift for bump positions near 90°, is significantly altered. The highest lift values resulted from a bump at less than 90°.

https://doi.org/10.1017/flo.2026.10042 Published online by Cambridge University Press

When the bump is sufficiently close to the stagnation point ($60° < \theta < 70°$), it acts as trip and further develops the already turbulent boundary layer. As a result, the final separation point moves to $90°$ compared with the case of no trip with separation at $120°$. In this range, the favourable pressure gradient after the bump is sufficiently strong so that the bump cannot remove the boundary layer from the surface. However, while separation does not occur on the bump, the separation point is moved upstream compared with the baseline case.

Across observations, drag was not found to be a strong function of the bump position outside the low drag observed at $\delta = 1.33\ \%$ and $\theta_b = 60°$. In this case, the bump did not fully separate the boundary layer. In addition, drag increased significantly with bump size.

Acknowledgements. We would like to thank Mr. Terry Zollinger for his assistance in the design and construction of the test article.

Data availability statement. Raw data are available from the corresponding author (J.E.).

Author contributions. J.E. conducted the experimental design, data collection, data analysis and co-drafted the initial manuscript. A.N. conducted pressure measurement data collection. B.L.S. conceived of the study, co-drafted the initial manuscript, advised on data collection and advised on data analysis. All authors participated in contributing to the initial and revised manuscript. All authors approve of the content in this manuscript and agree to be held accountable for the work.

Funding statement. This study was not funded.

Declaration of interests. The authors declare no conflict of interest.

Ethical standards. The research meets all ethical guidelines, including adherence to the legal requirements of the study country.

Appendix

The full non-transformed pressure data for the cylinder with the bump placed from $60° \leq \theta_b \leq 120°$ are provided.

https://doi.org/10.1017/flo.2026.10042 Published online by Cambridge University Press

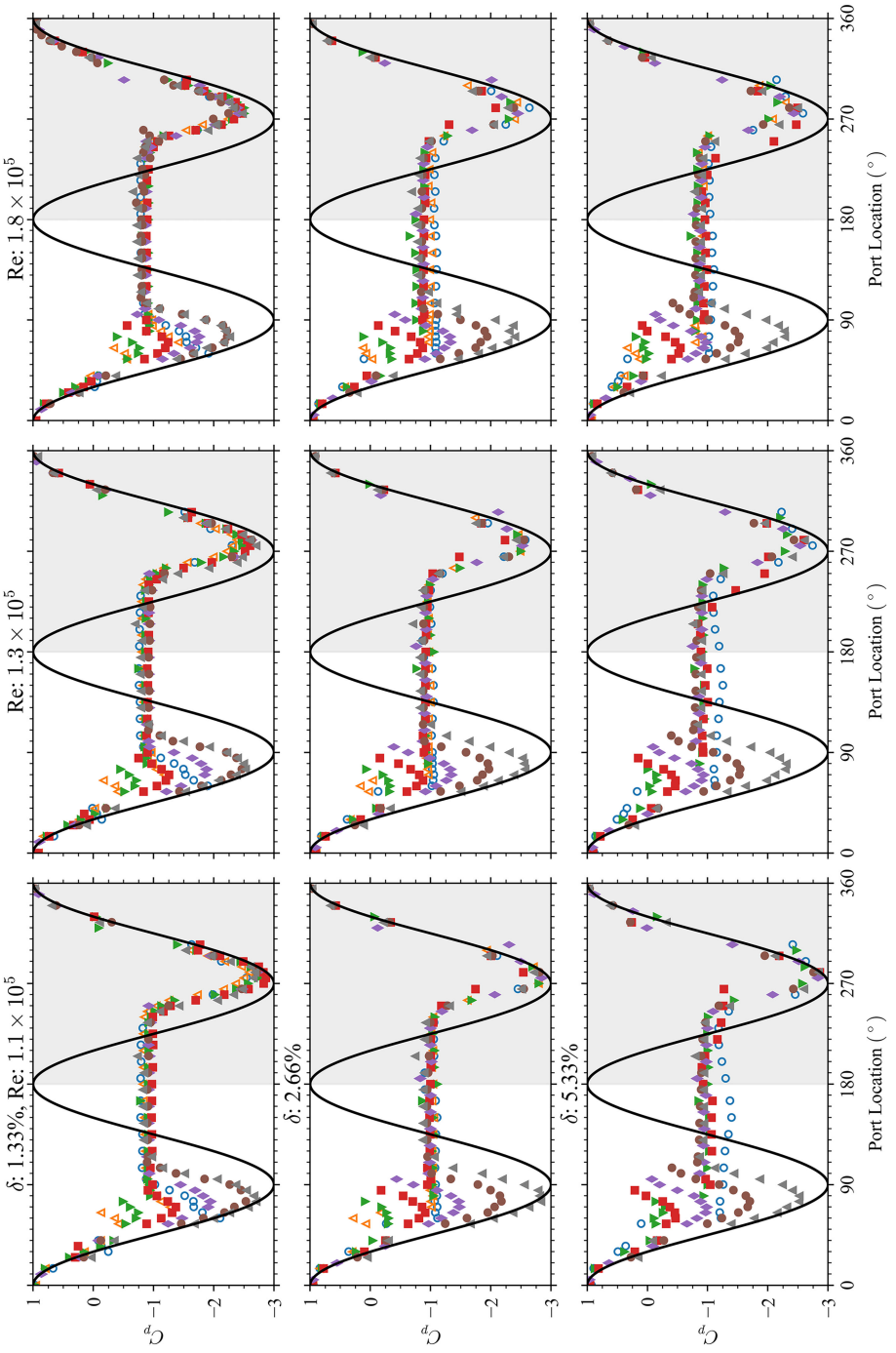


Figure A1. *Surface pressure coefficient as a function of angle with the bump at angles ranging from* 60° *to* 120° *for the three bumps and three values of Re. The bump positions are* 60° (○), 70° (△), 80° (▼), 90° (■), 100° (◆), 110° (●) *and* 120° (▲). *The grey-shaded region indicates the side of the cylinder with no bump. The line is the potential flow solution. Uncertainty bands are omitted to maintain readability.*

https://doi.org/10.1017/flo.2026.10042 Published online by Cambridge University Press

References

Achenbach, E. (1968). Distribution of local pressure and skin friction around a circular cylinder in cross-flow up to $Re = 5 \times 10^6$. *Journal of Fluid Mechanics*, *34*(4), 625–639. https://doi.org/10.1017/S0022112068002120

Achenbach, E. (1971). Experimental determination of momentum thickness of the circular cylinder in cross flow. *Journal of Fluid Mechanics*, *4*(1), 18–24. https://doi.org/10.1007/BF01002758

Achenbach, E. (1972). Experiments on the flow past spheres at very high Reynolds numbers. *Journal of Fluid Mechanics*, *54*(3), 10.

Barnes, C. J. (2024). Exploration of high-frequency actuation on gust response using large eddy simulation. *Journal of Fluids Engineering*, *146*(7), 071109. https://doi.org/10.1115/1.4065149

Bianchi, V., Silva, L. S. P., Cenci, F., Hirabayashi, S., Suzuki, H., & Gonçalves, R. T. (2020). Spoiler plate effects on the suppression of vortex-induced motions of a single circular cylinder. *Ocean Engineering*, *210*, 107569. https://doi.org/10.1016/j.oceaneng.2020.107569

Blaylock, M., Chow, R., Cooperman, A., & van Dam, C. P. (2014). Comparison of pneumatic jets and tabs for Active Aerodynamic Load Control. *Wind Energy*, *17*(9), 1365–1384. https://doi.org/10.1002/we.1638

Botros, K. K., Clavelle, E., & Satish, H. (2022). Insight into the interaction between flow field and acoustic field of turning flow into a side branch against a deadleg. *Journal of Fluids Engineering*, *144*(6), 061111. https://doi.org/10.1115/1.4054047

Bourgeois, J., & Houde, S. (2023). Investigations of spoilers to mitigate columnar vortices in propeller turbines at speed–no–load based on steady and unsteady flow simulations. *Journal of Fluids Engineering*, *145*(11), 111202. https://doi.org/10.1115/1.4062645

Briggs, L. J. (1959). Effect of spin and speed on the lateral deflection (curve) of a baseball; and the magnus effect for smooth spheres. *American Journal of Physics*, *27*(8), 589–596. https://doi.org/10.1119/1.1934921

Bruggeman, J. C., Hirschberg, A., van Dongen, M. E. H., Wijnands, A. P. J., & Gorter, J. (1989). Flow induced pulsations in gas transport systems: Analysis of the influence of closed side branches. *Journal of Fluids Engineering*, *111*(4), 484–491. https://doi.org/10.1115/1.3243672

Bruggeman, J. C., Hirschberg, A., van Dongen, M. E. H., Wijnands, A. P. J., & Gorter, J. (1991). Self-sustained aero-acoustic pulsations in gas transport systems: Experimental study of the influence of closed side branches. *Journal of Sound and Vibration*, *150*(3), 371–393. https://doi.org/10.1016/0022-460X(91)90893-O

Choi, H., Jeon, W.-P., & Kim, J. (2008). Control of flow over a bluff body. *Annual Review of Fluid Mechanics*, *40*(1), 113–139.

Chopra, G., & Mittal, S. (2022). The effect of trip wire on transition of boundary layer on a cylinder. *Physics of Fluids*, *34*(5), 054103. https://doi.org/10.1063/5.0089512

Coleman, H. W., & Steele, W. G. (2009). *Experimentation, validation, and uncertainty analysis for engineers* (3rd ed.). John Wiley and Sons.

Desai, A., Mittal, S., & Mittal, S. (2020). Experimental investigation of vortex shedding past a circular cylinder in the high subcritical regime. *Physics of Fluids*, *32*(1), 014105. https://doi.org/10.1063/1.5124168

Elliott, J., Smith, L., Lyu, B., & Smith, B. L. (2024). The combined influence of spin and roughness frequency on sphere aerodynamics. *Experiments in Fluids*, *65*(4), 60.

Farell, C., Guven, O., Carrasquel, S., & Patel, V. C. (1977). Effect of wind-tunnel walls on the flow past circular cylinders and cooling tower models. *Journal of Fluids Engineering*, *99*(3), 470–479. https://doi.org/10.1115/1.3448820

Gong, J., Wang, J., Liu, X., & Jiang, H. (2024). Numerical comprehensive evaluation of the flow control effect on a circular cylinder with a control rod. *Fluid Dynamics Research*, *56*(4), 045502.

Güven, O., Farell, C., & Patel, V. C. (1980). Surface-roughness effects on the mean flow past circular cylinders. *Journal of Fluid Mechanics*, *98*(4), 673–701. https://doi.org/10.1017/S0022112080000341

Heathcote, D. J., Gursul, I., & Cleaver, D. J. (2020). Dynamic deployment of a minitab for aerodynamic load control. *Journal of Aircraft*, *57*(1), 41–61. https://doi.org/10.2514/1.C035556

Igarashi, T. (1986). Effect of tripping wires on the flow around a circular cylinder normal to an airstream. *Bulletin of JSME*, *29*(255), 2917–2924. https://doi.org/10.1299/jsme1958.29.2917

Lin, S., Meng, H., Yang, W., & Gao, D. (2025). Experimental investigation on the aerodynamics and flow patterns of a 5:1 rectangular cylinder with spoilers. *Experimental Thermal and Fluid Science*, *160*, 111284.

Lyu, B., Smith, L., Elliott, J., & Kensrud, J. (2022). The dependence of baseball lift and drag on spin. *Proceedings of the Institution of Mechanical Engineers, Part P: Journal of Sports Engineering and Technology*, *239*(2), 235–241. https://doi.org/10.1177/17543371221113914

Maskell, E. C. (1963). A theory of the blockage effects on bluff bodies and stalled wings in a closed wind tunnel. British ARC, R&M 3400.

Nakamura, Y., & Tomonari, Y. (1982). The effects of surface roughness on the flow past circular cylinders at high Reynolds numbers. *Journal of Fluid Mechanics*, *123*, 363–378. https://doi.org/10.1017/S0022112082003103

Nebres, J., & Batill, S. (1993). Flow about a circular cylinder with a single large-scale surface perturbation. *Experiments in Fluids*, *15*(6), 369–379. https://doi.org/10.1007/BF00191775

Norman, A. K., & McKeon, B. J. (2011). The effect of a small isolated roughness element on the forces on a sphere in uniform flow. *Experiments in Fluids*, *51*(4), 1031–1045.

https://doi.org/10.1017/flo.2026.10042 Published online by Cambridge University Press

Pasam, A., Tudball Smith, D., Holmes, J. D., Burton, D., & Thompson, M. C. (2023). The influence of surface roughness on postcritical flow over circular cylinders revisited. *Journal of Fluid Mechanics*, *975*, A36. https://doi.org/10.1017/jfm.2023.846

Qian, Y., Wang, Z., & Gursul, I. (2023). Lift alleviation in travelling vortical gusts. *The Aeronautical Journal*, *127*(1316), 1676–1697. https://doi.org/10.1017/aer.2023.26

Seo, S.-H., Nam, C.-D., Han, J.-Y., & Hong, C.-H. (2013). Drag reduction of a bluff body by grooves laid out by design of experiment. *Journal of Fluids Engineering*, *135*(11), 111202. https://doi.org/10.1115/1.4024934

Smith, B. L., Garrett, J., Dufour, P., & Francis, E. (2024). How seams alter boundary layer separation points on baseballs. *Experiments in Fluids*, *65*(3), 27.

Smith, B. L., & Glezer, A. (1998). The formation and evolution of synthetic jets. *Physics of Fluids*, *10*(9), 2281–2297. https://doi.org/10.1063/1.869828

Smith, B. L., & Neal, D. R. (2025). *Measurement uncertainty*. Utah State University.

West, G. S., & Apelt, C. J. (1993). Measurements of fluctuating pressures and forces on a circular cylinder in the Reynolds number range 10^4 to 2.5×10^5. *Journal of Fluids and Structures*, *7*(3), 227–244. https://doi.org/10.1006/jfls.1993.1014

Yeung, W. W. H. (2009). On pressure invariance, wake width and drag prediction of a bluff body in confined flow. *Journal of Fluid Mechanics*, *622*, 321–344. https://doi.org/10.1017/S0022112008005247

Cite this article: Elliott J., Nielson A. and Smith B.L. (2026). Flow over a cylinder with a small triangular bump. *Flow*, *6*, E5. https://doi.org/10.1017/flo.2026.10042

https://doi.org/10.1017/flo.2026.10042 Published online by Cambridge University Press